

Quantitative Cerebral Blood Volume Image Synthesis from Standard MRI Using Image-to-Image Translation for Brain Tumors

Bao Wang, MD, PhD* • Yongsheng Pan, PhD* • Shangchen Xu, MD, PhD • Yi Zhang, MD, PhD • Yang Ming, MD, PhD • Ligang Chen, MD, PhD • Xuejun Liu, MD, PhD • Chengwei Wang, MD, PhD • Yingchao Liu, MD, PhD** • Yong Xia, PhD**

From the Department of Radiology, Qilu Hospital of Shandong University, Jinan, China (B.W.); School of Computer Science and Engineering, Northwestern Polytechnical University, Xi'an, China (Y.P., Y.X.); Departments of Neurosurgery (B.W., S.X., Y.L.) and Radiology (Y.Z.), Provincial Hospital Affiliated to Shandong First Medical University, Jinan 250021, China; Department of Neurosurgery, The Affiliated Hospital of Southwest Medical University, Luzhou, China (Y.M., L.C., Y.L.); Department of Radiology, The Affiliated Hospital of Qingdao University, Qingdao, China (X.L.); Department of Neurosurgery, the Second Hospital of Shandong University, Jinan, China (C.W.); and Shandong Institute of Brain Science and Brain-inspired Research, Shandong First Medical University, Jinan, China (Y.L.). Received September 27, 2022; revision requested December 12; revision received May 20, 2023; accepted June 9. Address correspondence to Y.L. (email: yingchaoliu@email.sdu.edu.cn).




Study supported in part by the Taishan Scholar Program (tsqn20161070), Natural Science Foundation of Shandong Province (grants ZR2019HM067, ZR2021QH125), Postdoctoral Science Foundation of China (grants BX2021333, 2021M703340), and National Natural Science Foundation of China (grants 82202114, U1806202).

* B.W. and Y.P. contributed equally to this work.

** Y.L. and Y.X. are co-senior authors.

Conflicts of interest are listed at the end of this article.

See also the editorial by Branstetter in this issue.

Radiology 2023; 308(2):e222471 • <https://doi.org/10.1148/radiol.222471> • Content codes:   

Background: Cerebral blood volume (CBV) maps derived from dynamic susceptibility contrast-enhanced (DSC) MRI are useful but not commonly available in clinical scenarios.

Purpose: To test image-to-image translation techniques for generating CBV maps from standard MRI sequences of brain tumors using the bookend technique DSC MRI as ground-truth references.

Materials and Methods: A total of 756 MRI examinations, including quantitative CBV maps produced from bookend DSC MRI, were included in this retrospective study. Two algorithms, the feature-consistency generative adversarial network (GAN) and three-dimensional encoder-decoder network with only mean absolute error loss, were trained to synthesize CBV maps. The performance of the two algorithms was evaluated quantitatively using the structural similarity index (SSIM) and qualitatively by two neuroradiologists using a four-point Likert scale. The clinical value of combining synthetic CBV maps and standard MRI scans of brain tumors was assessed in several clinical scenarios (tumor grading, prognosis prediction, differential diagnosis) using multicenter data sets (four external and one internal). Differences in diagnostic and predictive accuracy were tested using the z test.

Results: The three-dimensional encoder-decoder network with T1-weighted images, contrast-enhanced T1-weighted images, and apparent diffusion coefficient maps as the input achieved the highest synthetic performance (SSIM, $86.29\% \pm 4.30$). The mean qualitative score of the synthesized CBV maps by neuroradiologists was 2.63. Combining synthetic CBV with standard MRI improved the accuracy of grading gliomas (standard MRI scans area under the receiver operating characteristic curve [AUC], 0.707; standard MRI scans with CBV maps AUC, 0.857; $z = 15.17$; $P < .001$), prediction of prognosis in gliomas (standard MRI scans AUC, 0.654; standard MRI scans with CBV maps AUC, 0.793; $z = 9.62$; $P < .001$), and differential diagnosis between tumor recurrence and treatment response in gliomas (standard MRI scans AUC, 0.778; standard MRI scans with CBV maps AUC, 0.853; $z = 4.86$; $P < .001$) and brain metastases (standard MRI scans AUC, 0.749; standard MRI scans with CBV maps AUC, 0.857; $z = 6.13$; $P < .001$).

Conclusion: GAN image-to-image translation techniques produced accurate synthetic CBV maps from standard MRI scans, which could be used for improving the clinical evaluation of brain tumors.

Published under a CC BY 4.0 license.

Supplemental material is available for this article.

Cerebral blood volume (CBV) maps derived from dynamic susceptibility contrast-enhanced (DSC) MRI are an accepted and robust method for evaluating brain tumor perfusion (1). Despite the significance of CBV maps in clinical practice, there are challenges in their acquisition and application (2,3). The image-to-image translation technique, which aims to translate one visual representation or style to another visual representation or style or to build a map from a series of images to another, could potentially convert nonperfusion standard MRI scans into perfusion images (4,5).

A generative adversarial network (GAN) is a deep learning-based framework that learns mapping from a set of training data and generates synthetic data of the same characteristics as the training data (5). GANs consist of a generator and a discriminator, both of which are typically neural networks, competing against each other. The generator inputs source data and is trained to produce fake target data, whereas the discriminator is trained to distinguish the generated fake data from real target data. GAN and their variants

Abbreviations

ADC = apparent diffusion coefficient, AUC = area under the receiver operating characteristic curve, CBV = cerebral blood volume, DSC = dynamic susceptibility contrast enhanced, GAN = generative adversarial network, SCALE-PWI = self-calibrated echo-planar perfusion-weighted imaging, SSIM = structural similarity index

Summary

Generative adversarial network image-to-image translation techniques enabled the generation of accurate cerebral blood volume maps from standard MRI scans.

Key Results

- In this retrospective study of 370 patients with 756 MRI examinations, 529 for training models for quantitative cerebral blood volume (CBV) map synthesis and 227 for models' performance validation, a generative adversarial network–based deep learning algorithm achieved the best performance for synthesizing CBV maps using T1-weighted images, contrast-enhanced T1-weighted images, and apparent diffusion coefficient (ADC) maps (structural similarity index, $86.29\% \pm 4.30$).
- Combining synthetic CBV maps with standard MRI scans improved the accuracy of tumor grading in gliomas (standard MRI scans, 0.707; standard MRI scans with CBV maps, 0.857; $P < .001$), prediction of prognosis in gliomas (standard MRI scans, 0.654; standard MRI scans with CBV maps, 0.793; $P < .001$), and differentiation between tumor recurrence and treatment response in gliomas (standard MRI scans, 0.778; standard MRI scans with CBV maps, 0.853; $P < .001$) and brain metastases (standard MRI scans, 0.749; standard MRI scans with CBV maps, 0.857; $P < .001$).

have been widely applied in deep learning techniques for brain image synthesis (6,7). GAN-based techniques have previously been used in cross-modality image translation

and are promising for generating CBV maps from a series of MRI scans.

Unlike standard MRI scans, DSC MRI commonly requires manual postprocessing by experts (2), which may result in interoperator variability when generating CBV maps (8). For example, the value of a specific voxel may vary among CBV maps when different postprocessing protocols are used (9,10). The lack of standardized CBV maps with limited manual intervention may affect the ability of GAN-based techniques to synthesize accurate CBV maps. The bookend technique is a DSC MRI method that provides quantitative perfusion measurement with patient-specific calibration through an arterial input function–independent steady-state measurement of CBV, obtained from T1 value changes in the white matter and blood pool after contrast agent injection (11). Recently, an MRI pulse sequence (self-calibrated echo-planar perfusion-weighted imaging [SCALE-PWI]; 12), implementing the bookend technique, established an operator-independent generation of quantitative CBV maps, thus eliminating interoperator bias. The availability of reliable and operator-independent quantitative CBV maps used as ground-truth data may enable reliable synthesis of CBV maps using GAN-based techniques.

Our retrospective study aimed to investigate the feasibility of a GAN-based deep-learning algorithm for generating quantitative CBV maps from standard MRI scans with reference to quantitative CBV maps from SCALE-PWI. In addition, we aimed to evaluate the additional clinical value of synthetic CBV maps for assistance with brain tumor management of grading, differential diagnosis, and prognosis prediction using multicenter external data sets.

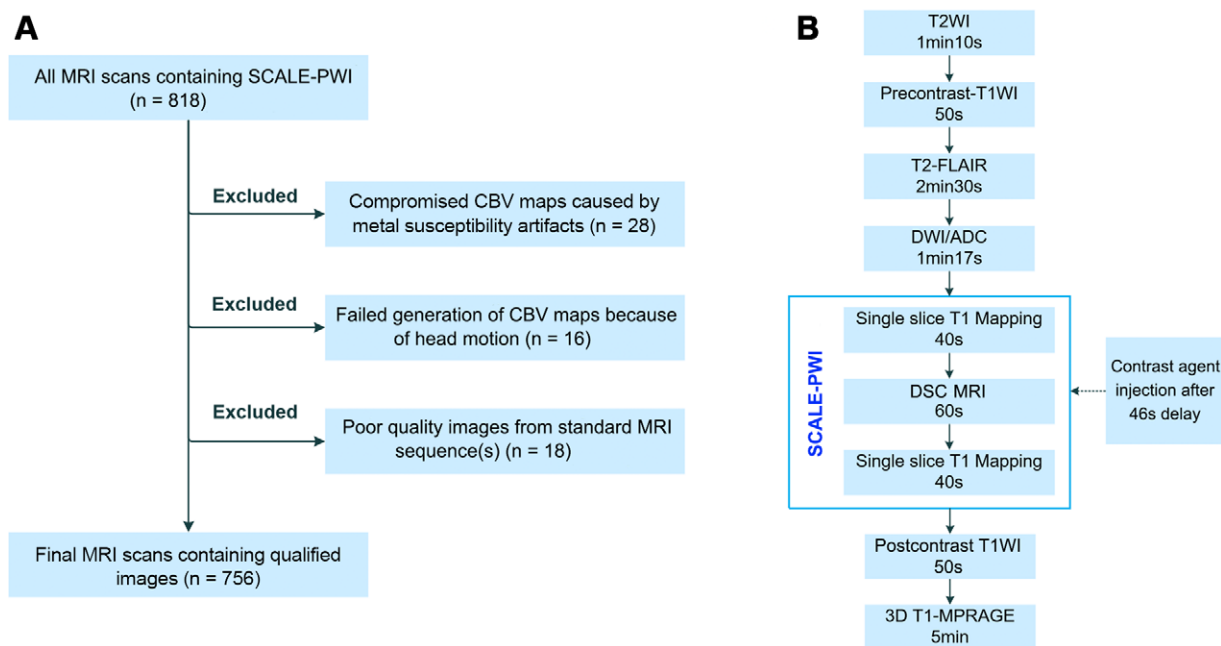


Figure 1: Data collection flow charts. **(A)** MRI scans screened for inclusion and final study sample and **(B)** sequence protocol with acquisition times. ADC = apparent diffusion coefficient, CBV = cerebral blood volume, DSC = dynamic susceptibility contrast, DWI = diffusion-weighted imaging, SCALE-PWI = self-calibrated echo-planar perfusion-weighted imaging, T1WI = T1-weighted image, T1-MPRAGE = T1-weighted magnetization prepared rapid gradient echo, T2-FLAIR = T2-weighted fluid-attenuated inversion recovery, T2WI = T2-weighted image, 3D = three-dimensional.

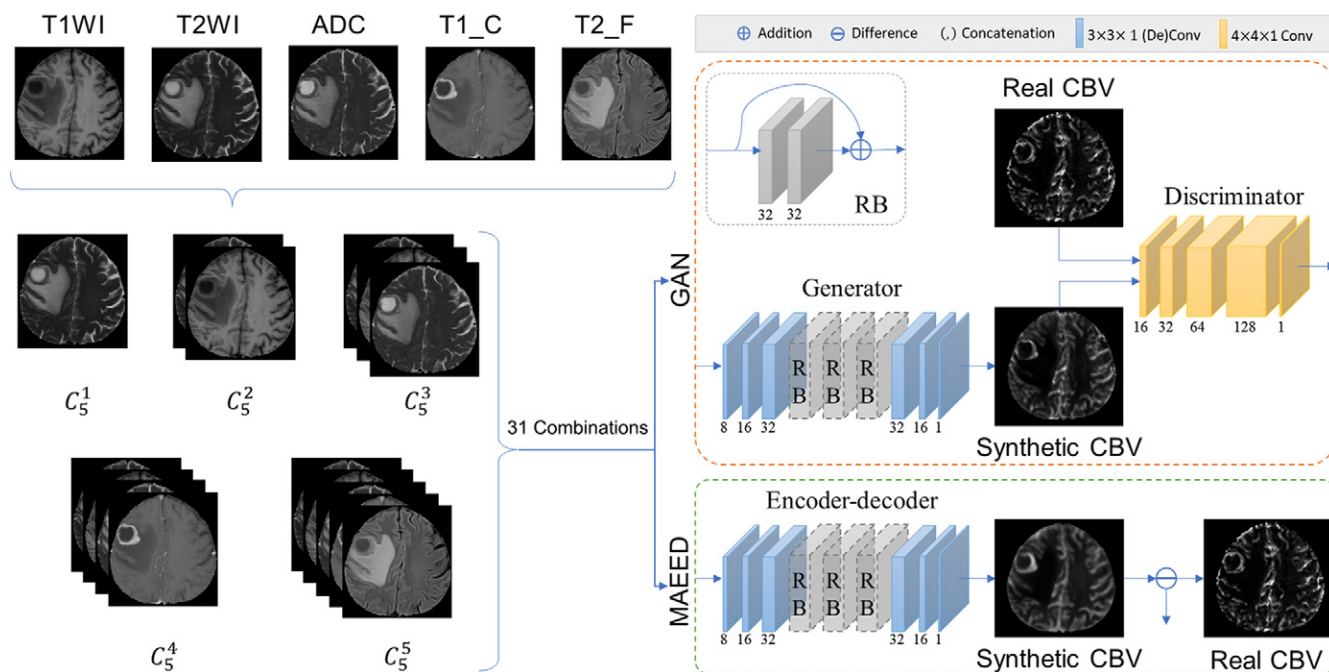


Figure 2: Flowchart for synthesizing cerebral blood volume (CBV) maps from standard MRI sequences using two deep learning algorithms. The left panel shows the input sequence combinations for the five MRI sequences. The right panel shows the two image synthesis algorithms. C_n^m , where n is 1–5, means selecting n kind (or kinds) of MRI sequence (or sequences) from all five kinds of MRI sequences. ADC = apparent diffusion coefficient, GAN = generative adversarial network, MAEED = three-dimensional encoder-decoder network for computing mean absolute error loss, RB = residual block, T1WI = T1-weighted image, T1_C = contrast-enhanced T1-weighted image, T2_F = T2-weighted fluid attenuated inversion recovery, T2WI = T2-weighted image.

Materials and Methods

Study Sample

In this retrospective study, MRI examinations of brain tumors that contained quantitative CBV maps using SCALE-PWI and that were performed between December 2016 and March 2020 were screened for inclusion. Inclusion criteria were as follows: (a) primary and recurrent brain tumors confirmed by pathologic results, (b) brain metastases confirmed by pathologic results, (c) follow-up MRI examinations available for patients in (a) and (b). Exclusion criteria were (a) compromised quality of CBV maps caused by metal susceptibility artifacts, (b) failed automatic generation of quantitative CBV maps because of registration errors from patient motion, (c) compromised image quality of standard MRI examinations, and (d) age younger than 18 years.

The study was approved by the local ethics committee (no. 2019–272). All experiments were performed in compliance with the Declaration of Helsinki. As a retrospective study, the requirement for informed consent was waived.

Image Acquisition and Preprocessing

The MRI workflow protocol is shown in Figure 1. Detailed information regarding MRI protocols, SCALE-PWI, and quantitative CBV maps are summarized in Appendix S1. The preprocessing steps are also shown Appendix S1.

GAN-based Techniques

MRI examinations were randomly assigned to a training set and a validation set at a 7:3 ratio. Two image-to-image translation techniques were used to test whether CBV volume could be synthesized

Table 1: Clinical Information of the Study Sample Used for Image-to-Image Translation

Parameter	Value
No. of patients	370
No. of MRI scans	756
Mean no. of scans per patient*	2.04 (1–7)
Mean age (y) [†]	58.73 ± 10.26
Sex	
Male	204 (55.1)
Female	166 (44.9)
Type of brain disease	
Glioma	134 (36.2)
Brain metastasis	183 (49.5)
Lymphoma	12 (3.2)
Meningioma	16 (4.3)
Medulloblastoma	14 (3.8)
Other [†]	11 (3.0)

Note.—There were 370 patients total. Unless otherwise indicated, data are numbers of patients; data in parentheses are percentages. Mean age is ± SD.

* Data in parentheses are ranges.

[†] Including solitary fibrous tumors, angiosarcoma, and germinomas.

from multiple MRI sequences: feature-consistency GAN (13) and three-dimensional encoder-decoder network with mean absolute error loss (14). Both algorithms were adapted to our SCALE-PWI data set by adopting two-dimensional convolutional layers but

Table 2: Results of 31 Generative Models of Two Algorithms

Sequence	Feature-consistency GAN SSIM (%)	Three-dimensional Encoder-Decoder MAE SSIM (%)
One MRI sequence		
T1	83.06 ± 4.20	83.51 ± 3.95
T2	82.61 ± 4.00	83.35 ± 3.97
Contrast-enhanced T1	85.76 ± 4.49	85.45 ± 4.18
T2-FLAIR	83.50 ± 3.95	83.72 ± 3.89
ADC	84.10 ± 4.18	84.18 ± 3.80
Two MRI sequences		
T1 with T2	83.88 ± 4.32	83.91 ± 4.01
T1 with contrast-enhanced T1	85.46 ± 4.33	85.32 ± 4.34
T1 with T2-FLAIR	83.53 ± 4.06	84.02 ± 4.01
T1 with ADC	84.02 ± 4.19	84.48 ± 3.94
T2 with contrast-enhanced T1	85.57 ± 4.38	86.07 ± 4.24
T2 with T2-FLAIR	83.62 ± 4.33	83.96 ± 3.73
T2 with ADC	83.89 ± 4.29	84.09 ± 4.13
contrast-enhanced T1 with T2-FLAIR	85.80 ± 4.63	85.51 ± 4.22
contrast-enhanced T1 with ADC	85.92 ± 4.59	86.10 ± 4.21
T2-FLAIR with ADC	84.34 ± 4.14	84.47 ± 3.81
Three MRI sequences		
T1 with T2 and contrast-enhanced T1	85.56 ± 4.44	85.90 ± 4.31
T1 with T2 and T2-FLAIR	84.10 ± 4.20	82.84 ± 4.11
T1 with T2 and ADC	84.27 ± 4.24	84.76 ± 4.09
T1 with contrast-enhanced T1 and T2-FLAIR	85.73 ± 4.68	85.56 ± 4.09
T1 with contrast-enhanced T1 and ADC	86.19 ± 4.56	86.29 ± 4.30
T1 with T2-FLAIR and ADC	84.42 ± 4.18	84.63 ± 4.23
T2 with contrast-enhanced T1 and T2-FLAIR	85.52 ± 4.58	85.80 ± 4.35
T2 with contrast-enhanced T1 and ADC	85.84 ± 4.46	86.06 ± 4.18
T2 with T2-FLAIR and ADC	84.38 ± 4.06	84.84 ± 3.75
contrast-enhanced T1, T2-FLAIR, and ADC	86.09 ± 4.45	86.07 ± 4.01
Four MRI sequences		
T1 with T2, contrast-enhanced T1, and T2-FLAIR	85.63 ± 4.16	85.79 ± 3.99
T1 with T2, contrast-enhanced T1, and ADC	85.88 ± 4.48	85.61 ± 4.31
T1 with T2, T2-FLAIR, and ADC	84.49 ± 4.23	84.31 ± 4.12
T1 with contrast-enhanced T1, T2-FLAIR, and ADC	85.69 ± 4.75	86.25 ± 4.20
T2 with contrast-enhanced T1, T2-FLAIR, and ADC	86.08 ± 4.69	86.21 ± 4.17
All MRI sequences		
T1 with T2, contrast-enhanced T1, T2-FLAIR, and ADC	85.73 ± 4.59	86.25 ± 4.17

Note.—Data are ± SDs. ADC = apparent diffusion coefficient, GAN = generative adversarial network, MAE = mean absolute error, SSIM = structural similarity index, T2-FLAIR = T2-weighted fluid attenuated inversion recovery.

performing instance normalization across all three axes. The codes were implemented using software (Python version 3.7.5, Python Software Foundation; with Tensorflow 2.5, Google), and had been uploaded in GitHub (https://github.com/Yongsheng-Pan/Bookend_DSC_Generation). They require the GNU general public license.

Generative model.—The generative model was composed of the encoding, transferring, and decoding parts. The encoding part used three convolutional layers (16, 32, and 64 channels) to extract information from the input image. The transfer part used six residual network blocks (15) to transfer information from the encoding part to the decoding part. The decoding part used two deconvolutional layers (with 16 and 32 channels) and one convolutional layer (with one channel) to construct the target image. All convolutional and deconvolutional layers had kernel sizes of $3 \times 3 \times 1$, followed by instance normalization, which was specifically designed to use our data with large section thickness (range, 6–8 mm). Preprocessed multiparametric MRI sequences were concatenated along the channel axis.

Discriminative model.—The discriminative model consisted of five convolutional layers (16, 32, 64, 128, and one channel). With kernel sizes of $4 \times 4 \times 1$ and instance normalization, the input of the discriminative model was a synthetic or real CBV image, whereas the output was a binary indicator of whether the input volume was synthetic or real.

Constraints of learning.—The generative model is referred to as the generator in feature-consistency GAN and the backbone in encoder-decoder with mean absolute error loss, whereas the discriminative model was only used as the discriminator in feature-consistency GAN. Mean absolute error loss is a low-level constraint that encourages a pair of synthetic CBV and real CBV images to be similar in each voxel, whereas feature consistency loss is a coarse-to-fine multilevel constraint to ensure that the features of a pair of synthetic CBV and real CBV images are similar when passing through each layer of the discriminative model.

Training details.—In this experiment, we adopted the Adam optimizer (16) by setting the batch size to 1, the learning rate to 0.001, and the number of epochs to 500. For each of the two algorithms, we tested all combinations of the five MRI sequences (ie, T1 weighted, T2 weighted, contrast-enhanced T1 weighted, T2-weighted fluid-attenuated inversion recovery, and apparent diffusion

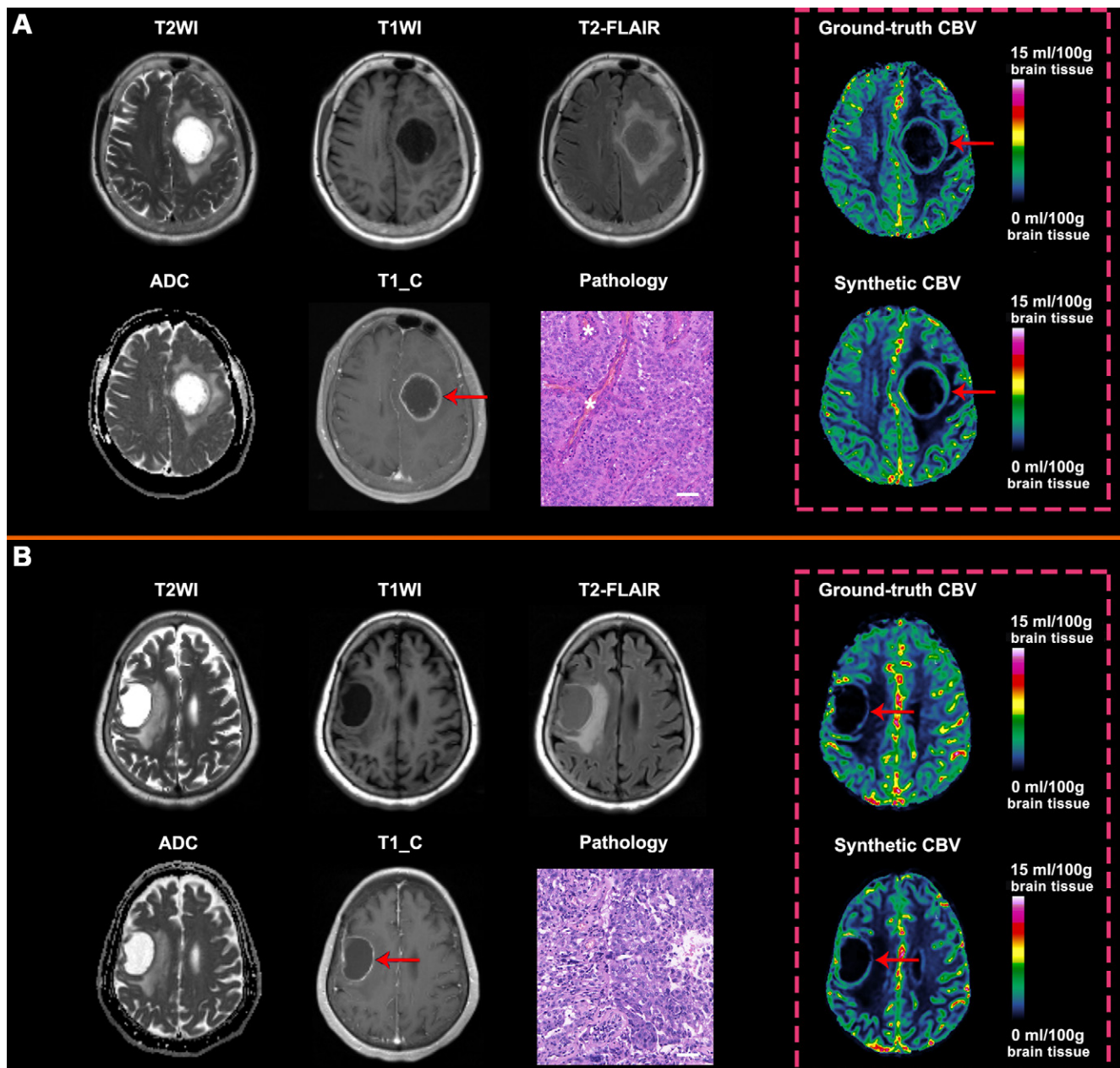


Figure 3: Standard MRI scans, pathology images, and ground-truth and synthetic cerebral blood volume (CBV) maps in patients with similar morphologic structure in tumor. **(A)** The standard MRI scans and quantitative CBV map were acquired in a 60-year-old patient with a ring-like lesion (arrows). The mean value of ground-truth CBV within the enhancing region was 5.2 mL per 100 g of brain tissue, and that of the synthetic CBV was 5.4 mL per 100 g of brain tissue. Hematoxylin-eosin staining in the pathology image shows the microvascular hyperplasia (*) but also the typical palisading necrosis, which is seen at the infiltrating edge of tumor enhancing rims and consist predominantly of rapidly dividing lumped endothelial cells, consistent with hyperperfusion glioblastoma. **(B)** The standard MRI scans and quantitative CBV map were acquired in a 70-year-old patient with a ring-like lesion (arrows). The mean value of ground-truth CBV within the enhanced region was 3.3 mL per 100 g of brain tissue, and that of the synthetic CBV was 3.6 mL per 100 g of brain tissue. Hematoxylin-eosin staining in the pathology image showed metastatic non-small cell lung cancer showing a prominent papillary architecture and adenoma morphologic cells surrounding fibrovascular cores with no typical vascular pattern, demonstrating its low hypoperfusion character. Magnification, $\times 300$; scale bar on pathologic image, 20 μm . ADC = apparent diffusion coefficient, T1WI = T1-weighted image, T1_C = contrast-enhanced T1-weighted image, T2-FLAIR = T2-weighted fluid attenuated inversion recovery, T2WI = T2-weighted image.

coefficient [ADC]). A flowchart showing the synthesis of CBV maps from standard MRI scans is shown in Figure 2.

Evaluation of Synthetic CBV Maps

For quantitative evaluation, we used the structure similarity index measure (SSIM) (17) to evaluate the quality of synthetic

CBV maps. The SSIM is considered to be more comparable to subjective evaluation. The SSIM quality assessment index is based on the computation of three terms: luminance, contrast, and structure. The overall index is a multiplicative combination of these three terms. Let I_r and I_p be a pair of real and synthetic images, respectively; then, SSIM is calculated as

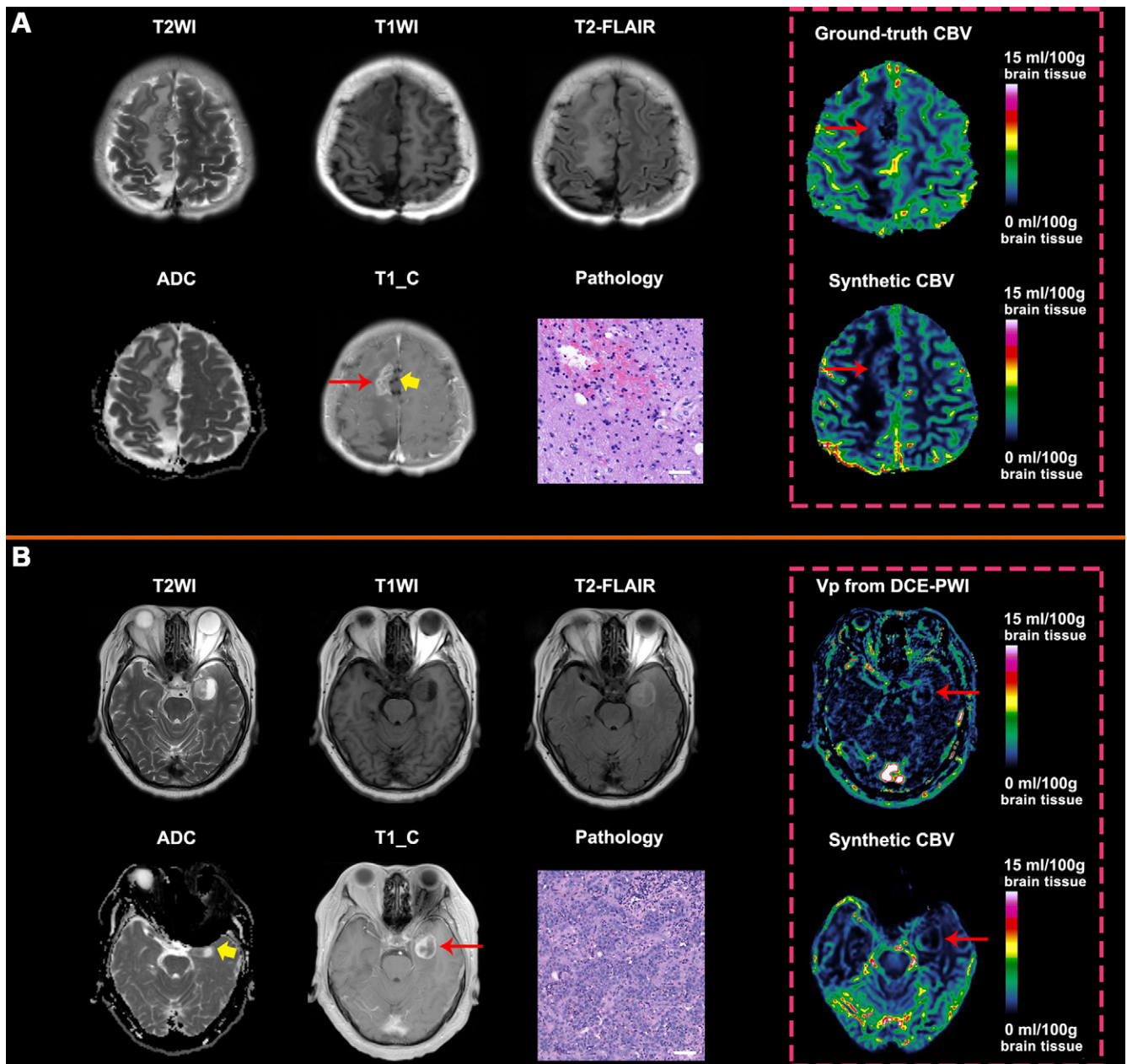


Figure 4: Standard MRI scans, pathology images, and ground-truth and synthetic cerebral blood volume (CBV) maps in patients with metal artifacts. **(A)** Images in a 20-year-old patient was diagnosed with a germ cell tumor along the falx cerebri, and radioactive particles (yellow arrow) were placed into the tumor. Five months later, a new focus of contrast enhancement (red arrows) was seen near the tumor. The radioactive particles led to focal signal loss. The synthetic CBV map shows a mean value of synthetic CBV within the enhancing region of 1.8 mL/100 g brain tissue. The hypoperfusion indicates it may be radiation necrosis. Hematoxylin-eosin stain showed a large area of noninflammatory fibrinoid vascular necrosis. No evidence of vascular proliferation is shown, consistent with hypoperfusion radiation therapy induced radiation necrosis. **(B)** Images in a 47-year-old patient with a solid-cystic lesion (red arrows) in the left temporal lobe. Metal dental material caused degradation of the gradient-echo images (apparent diffusion coefficient [ADC] and CBV images). Dynamic contrast-enhanced (DCE) MRI was used instead of dynamic susceptibility contrast MRI. Mean value of the vascular fraction of the tissue (Vp) within the enhanced region was 0.21, and that of synthetic CBV was 2.3 mL per 100 g of brain tissue, both of which indicate a hypoperfused lesion. Hematoxylin-eosin staining in the pathology image shows a prominent papillary architecture with foci of tumor necrosis, however, typical vascular hyperplasia is not shown (with only mild angiogenesis), confirming the lower hypoperfusion of brain metastasis from lung cancer. Magnification, $\times 300$; scale bar on pathologic image, 20 μm . PWI = perfusion-weighted imaging, T1WI = T1-weighted image, T1_C = contrast-enhanced T1-weighted image, T2-FLAIR = T2-weighted fluid attenuated inversion recovery, T2WI = T2-weighted image.

$$SSIM = \frac{(2\mu_r\mu_p + C_1)(2\sigma_{rp} + C_2)}{(\mu_r^2 + \mu_p^2 + C_1)(\sigma_r^2 + \sigma_p^2 + C_2)},$$

where μ_r , μ_p , σ_r , σ_p , and σ_{rp} are the local means, SDs, and cross-covariance for images I_r and I_p . $[C_1 = (0.01 \cdot R)^2]$ and $[C_2 =$

$(0.03 \cdot R)^2]$ are the specified parameters to avoid instability (R is dynamic range of voxel intensities). The range of the SSIM is 0–1, and a larger value indicates better image quality.

For qualitative evaluation, readings were randomly assigned to two neuroradiologists (Y.Z. and X.L., with 10 and 12 years of experience in MRI perfusion, respectively) who

Table 3: Comparisons of Glioma Grading and Prediction of Prognosis between Standard MRI and Standard MRI with Synthetic Cerebral Blood Volume Maps

Parameter	AUC			Category-Free Net Reclassification Index		Integrated Discrimination Improvement Analyses	
	Value	<i>z</i> Value	<i>P</i> Value	<i>z</i> Value	<i>P</i> Value	<i>z</i> Value	<i>P</i> Value
Glioma grading							
Standard MRI scans (reference)*	0.707 (0.686, 0.728)
Standard MRI scans with synthetic CBV maps	0.857 (0.806, 0.842)	15.17	<.001	14.24	<.001	15.17	<.001
Prognostic prediction							
Standard MRI scans (reference)*	0.654 (0.613, 0.692)
Standard MRI scans with synthetic CBV maps	0.793 (0.757, 0.825)	9.62	<.001	8.94	<.001	9.62	<.001

Note.—Data in parentheses are 95% CIs. Adjusted *P* values are shown after Bonferroni correction. AUC = area under the receiver operating characteristic curve, CBV = cerebral blood volume.

* Standard MRI included T1-weighted, T2-weighted, contrast-enhanced T1-weighted, T2-weighted fluid-attenuated inversion recovery images, and apparent diffusion coefficient.

independently evaluated the quality of the synthetic CBV map compared with the ground-truth CBV map. Synthetic CBV maps were scored on a four-point scale (0, very poor; 1, poor; 2, good; and 3, very good) for the following criteria: overall perfusion distribution of the lesions, overall perfusion degree of the lesions, and border and shape of the lesion. If divergencies existed, these two radiologists discussed and reached a consensus. The initial scores were also recorded for consistent evaluation.

Validation of the Value of Synthetic CBV Maps in Clinical Practice

We evaluated the value of synthetic CBV maps for three clinical scenarios using external data sets: grading of gliomas, prediction of prognosis of gliomas, and discrimination between tumor recurrence and treatment response. The values of standard MRI scans (T1-weighted images, T2-weighted images, contrast-enhanced T1-weighted images, and T2-weighted fluid-attenuated inversion recovery images, as well as ADC maps) and standard MRI scans with their synthetic CBV maps were compared for three clinical applications. The collection of external test data and detailed evaluation methods are provided in Appendix S1.

Statistical Analysis

Because multiple MRI examinations were performed in the same patients, within-group interrater reliability statistic (*r*) was performed to evaluate interobserver agreement regarding image quality scores. The level of reliability was considered very good at a within-group *r* value of at least 0.9, good at 0.70–0.89, fair at 0.50–0.69, and poor at 0.49 or less. The mean value of the image quality scores represents the final quality of all the synthetic CBV maps in qualitative evaluation. For quantitative image quality evaluation, the differences in SSIM between the two models were compared using a paired *t* test. Survival events were defined as death from any cause, and overall survival was calculated from the time of histologic diagnosis of the tumor.

The κ coefficient was used to evaluate the interobserver agreement regarding possible grading, survival prediction, and differential diagnosis. The level of agreement is the same as within-group *r*. The area under the receiver operating characteristic curve (AUC) for each model (standard MRI scans vs standard MRI scans with synthetic CBV maps) was calculated and compared for statistical significance. We also conducted category-free net reclassification index and integrated discrimination improvement analyses for further support. Bonferroni correction was applied to correct for multiple comparisons. A two-sided *P* < .05 indicated statistically significant differences. Statistical analyses were performed (B.W., with 6 years of experience) by using software (R version 3.2.0, www.r-project.org; and Matlab version 2021a, MathWorks).

Results

Study Sample

Of the 818 MRI examinations (422 patients, mean age, 59.3 years \pm 10.8; age range, 18–75 years; 224 male patients), including quantitative CBV maps, 28 (3.4%) were excluded because of compromised image quality of the quantitative CBV maps caused by metal susceptibility artifacts, 16 (2.0%) MRI examinations were excluded because of failed automatic generation of the quantitative CBV maps due to a registration error from patient head motion, and 18 (2.2%) MRI examinations were excluded because of compromised image quality of standard MRI sequences. Finally, 756 (92.4%) MRI examinations from 370 patients (mean age, 58.7 years \pm 10.3; age range, 18–75 years; 204 male participants) were included in this study. The study sample is shown in Figure 1. Detailed information regarding the study sample is summarized in Table 1.

Quantitative Evaluation of the Synthesized CBV

The results of the 31 generative models for the two algorithms in the validation cohort are summarized in Table 2. The three-dimensional encoder-decoder network for computing mean

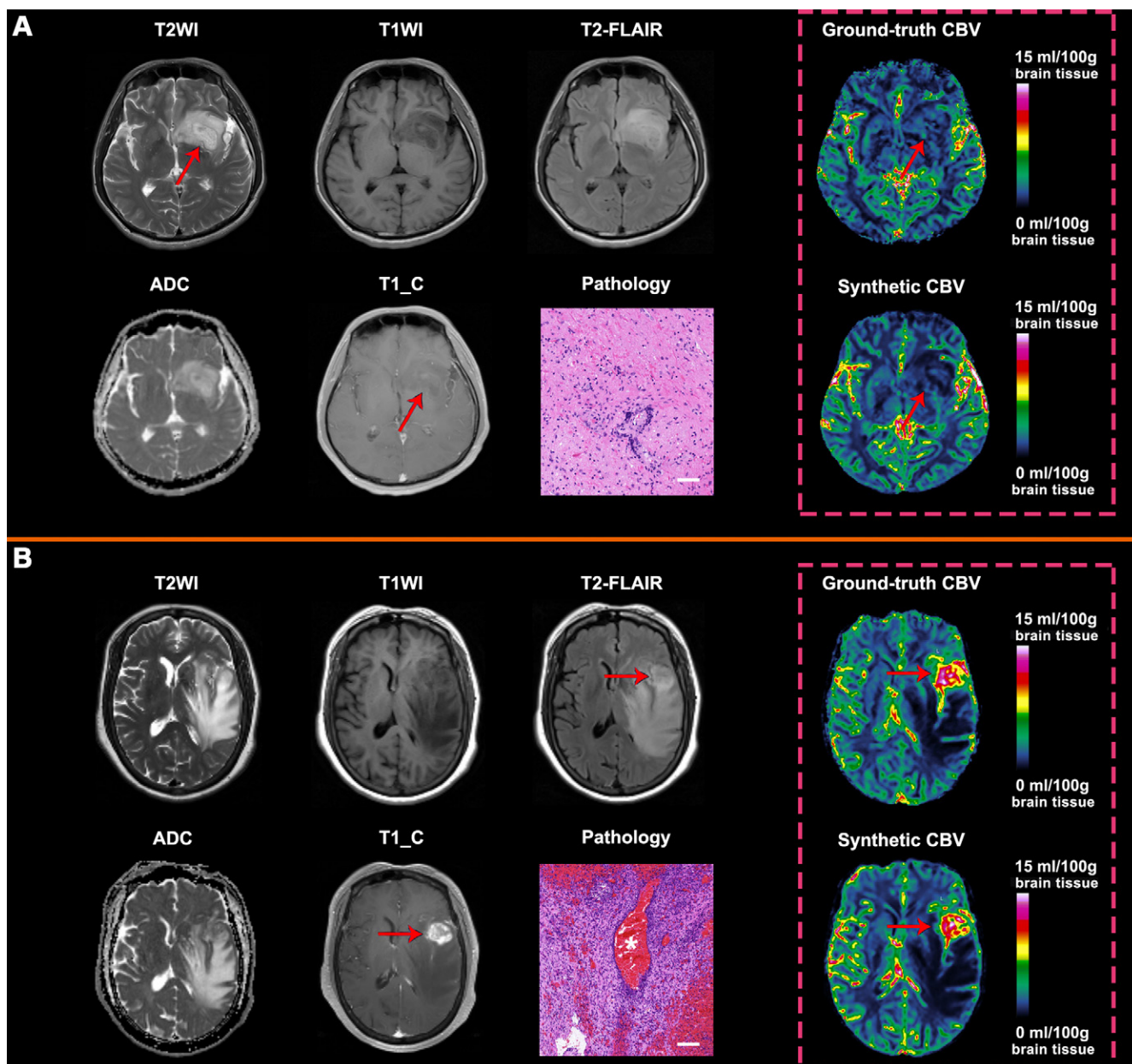


Figure 5: Standard MRI scans, pathology images, and ground-truth and synthetic cerebral blood volume (CBV) maps of patients diagnosed with low- and high-grade glioma. **(A)** The standard MRI scans and quantitative CBV map were acquired in a 45-year-old patient with a contrast-unenhanced lesion (arrow); the mean value of ground-truth CBV within the enhanced region was 2.1 mL per 100 g of brain tissue, and that of synthetic CBV was 1.9 mL per 100 g of brain tissue. Hematoxylin-eosin staining in pathology image shows modestly increased cellularity due to the presence of neoplastic cells. The vascular pattern distribution of the lesion was nearly normal, with no evidence of vascular proliferation, consistent with hypoperfusion low-grade glioma. **(B)** Standard MRI scans and quantitative CBV map in a 66-year-old patient with a contrast-enhanced lesion. The mean value of ground-truth CBV within the enhanced region (arrow) was 13.3 mL per 100 g of brain tissue, and that of synthetic CBV was 13.0 mL per 100 g of brain tissue. Hematoxylin-eosin staining on the pathology image shows microvascular hyperplasia (*) and typical palisading necrosis, which is shown at the infiltrating edge of enhancing tumor rims, consistent with hyperperfusion glioblastoma. Magnification, $\times 300$; scale bar on pathologic image, 20 μm . ADC = apparent diffusion coefficient, T1WI = T1-weighted image, T1_C = contrast-enhanced T1-weighted image, T2-FLAIR = T2-weighted fluid attenuated inversion recovery, T2WI = T2-weighted image.

absolute error loss using T1-weighted images, contrast-enhanced T1-weighted images, and ADC maps appeared to achieve the best performance among the 31 generative models (SSIM, 86.29 ± 4.30 , based on descriptive comparison only). Synthetic CBV maps derived from this model demonstrated the difference in perfusion between two tumors with similar morphologic structure, and examples are shown in Figure 3. The best performance of feature-consistency GAN was achieved using T1-weighted

images, contrast-enhanced T1-weighted images, and ADC maps (SSIM, 86.19 ± 4.56 , $P = .28$ [compared with the best model]).

Feature-consistency GAN using T2-weighted images showed the worst performance (SSIM, $82.61\% \pm 4.00$; $P < .001$). Furthermore, using all MRI sequences achieved a similar performance to the best model (SSIM, $86.25\% \pm 4.17$; $P = .46$). Specifically, feature-consistency GAN using contrast-enhanced T1 with T2-weighted fluid-attenuated inversion recovery showed

Table 4: Comparisons of Differentiation between Tumor Recurrence and Treatment Response between Standard MRI scans and Standard MRI Scans with Synthetic Cerebral Blood Volume Maps

Parameter	AUC			Category-Free Net Reclassification Index		Integrated Discrimination Improvement Analyses	
	Value	<i>z</i> Value	<i>P</i> Value	<i>z</i> Value	<i>P</i> Value	<i>z</i> Value	<i>P</i> Value
Glioma							
Standard MRI (reference)*	0.778 (0.727, 0.825)
Standard MRI scans with synthetic CBV maps	0.853 (0.808, 0.892)	4.86	<.001	4.69	<.001	4.86	<.001
Brain metastases							
Standard MRI scans (reference)*	0.749 (0.698, 0.796)
Standard MRI scans with synthetic CBV maps	0.857 (0.813, 0.893)	6.131	<.001	5.81	<.001	6.13	<.001

Note.—Data in parentheses are 95% CIs. Adjusted *P* values are shown after Bonferroni correction. AUC = area under the receiver operating characteristic curve, CBV = cerebral blood volume.

* Standard MRI included T1-weighted, T2-weighted, contrast-enhanced T1-weighted, T2-weighted fluid-attenuated inversion recovery images, and apparent diffusion coefficient.

the best performance (SSIM, 85.80% \pm 4.63; *P* = .008) among models without ADC maps (susceptible to metal artifact). Examples of clinical utility are shown in Figure 4.

Qualitative Evaluation of the Synthesized CBV

Synthetic CBV maps from the three-dimensional encoder-decoder network for computing mean absolute error loss using T1-weighted images, contrast-enhanced T1-weighted images, and ADC maps were used for qualitative evaluations. The interobserver agreement regarding the quality of the synthetic CBV maps was good (within-group *r* = 0.88). The mean image quality score for all the synthetic CBV maps was 2.63. For image quality scores, the percentages of those images rated as 1 point (poor quality), 2 points (good quality), and 3 points (very good quality) were 3.6% (27 of 756), 29.6% (224 of 756), and 66.8% (505 of 756), respectively.

Validation of the Values of Synthetic CBV Map in Clinical Practice

Of the 1792 included gliomas, 767 (42.8%) were low-grade gliomas and 1025 (57.2%) were high-grade gliomas. The combination of synthetic CBV and standard MRI improved glioma grading accuracy (standard MRI scans AUC, 0.707 [95% CI: 0.686, 0.728]; standard MRI scans with CBV maps AUC, 0.857 [95% CI: 0.806, 0.842]; *z* = 15.17; *P* < .001; Table 3), and there was very good agreement between the two evaluations (κ = 0.91; 95% CI: 0.83, 0.98). Examples of low-grade and high-grade gliomas are shown in Figure 5. Regarding the prediction of prognosis, among the 575 patients with survival data, 354 died during follow-up (median survival, 17.3 months; range: 3.4–74.7 months). The median length of follow-up for survivors was 34.2 months (range, 4.3–92.8 months). Compared with standard MRI, combining synthetic CBV and standard MRI improved prognostic prediction accuracy (standard MRI scans AUC, 0.654 [95% CI: 0.613, 0.692]; standard MRI scans with CBV maps AUC, 0.793 [95% CI: 0.757, 0.825]; *z* = 9.62; *P* < .001; Table 3),

with good agreement between the two evaluations (κ = 0.88; 95% CI: 0.80, 0.96).

Of the 294 patients with glioma suspected of recurrence versus treatment response, 158 (53.7%) were diagnosed with tumor recurrence and 136 (46.3%) were diagnosed with treatment response. Adding synthetic CBV to standard MRI significantly improved the accuracy of differentiating recurrence from treatment response in gliomas (standard MRI scans AUC, 0.778 [95% CI: 0.727, 0.825]; standard MRI scans with CBV maps AUC, 0.853 [95% CI: 0.808, 0.892]; *z* = 4.86; *P* < .001; Table 4). Examples of recurrence and treatment response in gliomas are shown in Figure 6. Of 320 patients with brain metastases suspected of having recurrence versus treatment response, 180 (56.3%) were diagnosed with tumor recurrence and 140 (43.7%) were diagnosed with treatment response. Adding synthetic CBV to standard MRI significantly improved the accuracy of differential diagnosis between recurrence and treatment response in brain metastases (standard MRI scans AUC, 0.749 [95% CI: 0.698, 0.796]; standard MRI scans with CBV maps AUC, 0.857 [95% CI: 0.813, 0.893]; *z* = 6.13; *P* < .001; Table 4). The overall agreement between the two evaluations of differential diagnosis in glioma and brain metastases was good (κ = 0.89; 95% CI: 0.82, 0.97).

Discussion

A salvage cerebral blood volume (CBV) map synthesized from standard MRI would be helpful in the precise treatment of brain tumors when dynamic susceptibility contrast (DSC) MRI is absent or has compromised image quality. In this study, we presented a generative adversarial network–based image synthesis method for creating a quantitative CBV map from standard MRI using bookend DSC MRI as the model training reference. The synthetic CBV maps not only demonstrated a similar appearance to the real quantitative CBV maps (structural similarity index, 86.29% \pm 4.30), but also showed feasible additional clinical values in tumor grading (*P* < .001) and prediction of prognosis (*P* < .001) of gliomas and differentiating tumor recurrence

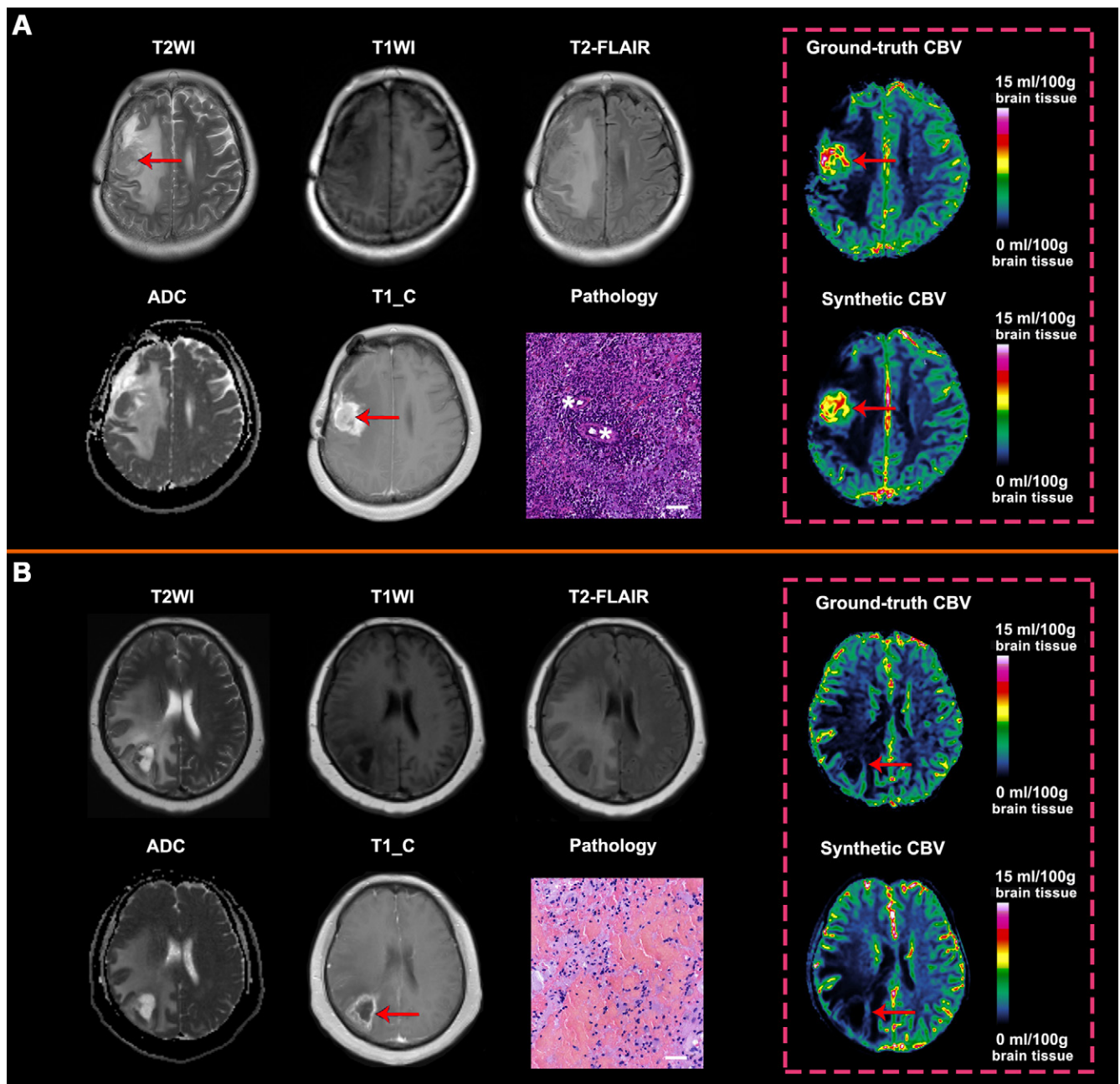


Figure 6: Standard MRI scans, pathology images, and ground-truth and synthetic cerebral blood volume (CBV) maps in patients diagnosed with recurrent glioblastoma and radiation necrosis. **(A)** Images in a 50-year-old patient who was diagnosed with glioblastoma underwent both radiation therapy and chemotherapy after tumor resection; 5 months later, a contrast-enhanced area (arrows) appeared in the irradiated region. The mean value of ground-truth CBV within the enhanced region was 10.3 mL per 100 g of brain tissue, and that of synthetic CBV was 9.8 mL per 100 g of brain tissue. Hematoxylin-eosin staining showed marked cellularity and typical microvascular hyperplasia characterized by small multilayered vessels (*), consistent with hyperperfusion tumor recurrence and progression. **(B)** Images in a 58-year-old patient with brain metastasis from kidney cancer underwent radiation therapy and chemotherapy; 5 months later, the contrast-enhanced region (arrows) had enlarged more than 50% compared with the previous follow-up MRI scans. The mean value of ground-truth CBV within the enhanced region was 1.2 mL per 100 g of brain tissue, and that of synthetic CBV was 1.0 mL per 100 g of brain tissue. Hematoxylin-eosin staining in the brain biopsy sample from this patient showed extensive fibrinoid parenchymal damage and large zones of coagulative vascular necrosis, consistent with hypoperfusion radiation necrosis. Magnification, $\times 300$; scale bar on pathologic image, 20 μm . ADC = apparent diffusion coefficient, T1WI = T1-weighted image, T1_C = contrast-enhanced T1-weighted image, T2-FLAIR = T2-weighted fluid attenuated inversion recovery, T2WI = T2-weighted image.

versus treatment response in gliomas and brain metastases (both $P < .001$) when the synthetic CBV maps were added to standard MRI scans.

Unlike the relative CBV maps derived from commonly used DSC MRI, the CBV maps derived from SCALE-PWI (with a bookend DSC MRI technique) were not only

quantitative but also operator independent (12), ensuring the standardization of output CBV maps. A study by Sanders et al (18) showed that realistic relative CBV maps can be synthesized from dynamic contrast-enhanced MRI and contain quantitative information. In this study, however, these relative CBV maps were generated from another brain perfusion

sequences, instead of anatomic MRI sequences, which could be more challenging due to the image translation across different domains. In addition, in the study by Sanders et al, both the real relative CBV maps and blood plasma volume fraction maps were manually processed, which inevitably introduces potential interoperator bias.

Relative CBV maps derived from DSC MRI have been found to be useful for tumor grading, prediction of prognosis, and differentiating between tumor recurrence and radiation necrosis (19). DSC MRI may not be performed routinely at the initial examination, although it has historically been recommended to clinicians (20). Therefore, an artificial CBV map that is synthesized using standard MRI scans would be convenient for diagnostic decision-making.

Our results demonstrated that the feature-consistency GAN using MRI sequences that are insusceptible to metal artifacts can generate CBV maps (SSIM, $85.80\% \pm 4.63$), providing a possible solution for DSC MRI with compromised image quality. Dynamic contrast-enhanced MRI (21) and arterial spin labeling perfusion (22) are alternative solutions for when DSC MRI is absent or has compromised image quality because they are less susceptible to artifacts. However, dynamic contrast-enhanced MRI requires administration of a gadolinium-based contrast agent and can be biased by poor measurement of the vascular input function and varied pharmacokinetic models (23). Arterial spin labeling requires a relatively long scanning time and has limited spatial resolution and signal-to-noise ratio (22).

Our study had several limitations. First, all gliomas were diagnosed and classified based on histopathologic structure instead of an integrative diagnosis of histologic structure and molecular markers as defined in the World Health Organization 2021 classification of tumors of central nervous system. Second, the performance of synthetic CBV maps was not directly compared with the real CBV maps. Third, the voxel intensity of contrast-enhanced T1-weighted images was mostly influenced by the acquisition point after contrast agent administration. These points vary among institutions, which may decrease the performance of our GAN-based techniques. Fourth, the state-of-the-art diffusion models could achieve superior performance in image synthesis compared with GAN models (24), but this study did not seek to explore the performance of diffusion models because of their high computational cost. Finally, SCALE-PWI with an arterial input function-independent, steady-state measurement of CBV was crucial for standardizing synthetic CBV maps production, but this was validated only in a monocentric setting because of its limited accessibility, which may limit the generalization of the method.

In conclusion, we used quantitative cerebral blood volume (CBV) maps derived from bookend dynamic susceptibility contrast-enhanced MRI scans to train and validate generative adversarial network-based CBV maps synthesized from standard MRI scans. Our results demonstrate that this structural image-to-functional image translation method can generate realistic quantitative CBV maps for improving clinical evaluation of brain tumors in the absence of dynamic susceptibility contrast MRI scans. We anticipate that a simple and

automatic end-to-end online image synthesis process will be required to enable broader dissemination and utilization in brain tumor treatment.

Acknowledgment: We thank the permission for SCALE-PWI from Siemens Healthineers. We thank Tao Zhang, PhD, from the School of Public Health of Shandong University for valuable statistical analysis support. We thank Senior Research Associate Chao Li, PhD, from the Department of Applied Mathematics and Theoretical Physics (DAMTP) and Clinical Neurosciences, University of Cambridge for his constructive suggestions.

Author contributions: Guarantors of integrity of entire study, B.W., Y.P., Y.Z., X.L., Y.L., Y.X.; study concepts/study design or data acquisition or data analysis/interpretation, all authors; manuscript drafting or manuscript revision for important intellectual content, all authors; approval of final version of submitted manuscript, all authors; agrees to ensure any questions related to the work are appropriately resolved, all authors; literature research, Y.M., L.C., X.L., Y.L., Y.X.; clinical studies, B.W., S.X., Y.Z., Y.M., L.C., X.L., C.W., Y.L.; experimental studies, B.W., Y.P., L.C., X.L., C.W.; statistical analysis, Y.P., S.X., Y.Z., L.C., X.L., Y.X.; and manuscript editing, B.W., Y.P., Y.Z., L.C., X.L., Y.L., Y.X.

Data sharing: Data generated or analyzed during the study are available from the corresponding author by request.

Disclosures of conflicts of interest: B.W. No relevant relationships. Y.P. No relevant relationships. S.X. No relevant relationships. Y.Z. No relevant relationships. Y.M. No relevant relationships. L.C. No relevant relationships. X.L. No relevant relationships. C.W. No relevant relationships. Y.L. No relevant relationships. Y.X. No relevant relationships.

References

- Kaufmann TJ. A new study in contrasts: brain MRI for the depiction of tumor metabolism. *Neuro-oncol* 2019;21(9):1095–1096.
- Essig M, Shiroishi MS, Nguyen TB, et al. Perfusion MRI: the five most frequently asked technical questions. *AJR Am J Roentgenol* 2013;200(1):24–34.
- Viallon M, Cuvinciuc V, Delattre B, et al. State-of-the-art MRI techniques in neuroradiology: principles, pitfalls, and clinical applications. *Neuroradiology* 2015;57(5):441–467. [Published correction appears in *Neuroradiology* 2015;57(10):1075.]
- Zaharchuk G, Gong E, Wintermark M, Rubin D, Langlotz CP. Deep Learning in Neuroradiology. *AJNR Am J Neuroradiol* 2018;39(10):1776–1784.
- Yi X, Walia E, Babyn P. Generative adversarial network in medical imaging: A review. *Med Image Anal* 2019;58:101552.
- Liu Y, Chen A, Shi H, et al. CT synthesis from MRI using multi-cycle GAN for head-and-neck radiation therapy. *Comput Med Imaging Graph* 2021;91:101953.
- Pan Y, Liu M, Xia Y, Shen D. Disease-Image-Specific Learning for Diagnosis-Oriented Neuroimage Synthesis With Incomplete Multi-Modality Data. *IEEE Trans Pattern Anal Mach Intell* 2022;44(10):6839–6853.
- Calamante F. Arterial input function in perfusion MRI: a comprehensive review. *Prog Nucl Magn Reson Spectrosc* 2013;74:1–32.
- Paulson ES, Schmainda KM. Comparison of dynamic susceptibility-weighted contrast-enhanced MR methods: recommendations for measuring relative cerebral blood volume in brain tumors. *Radiology* 2008;249(2):601–613.
- Prah MA, Stufflebeam SM, Paulson ES, et al. Repeatability of Standardized and Normalized Relative CBV in Patients with Newly Diagnosed Glioblastoma. *AJNR Am J Neuroradiol* 2015;36(9):1654–1661.
- Shin W, Cashen TA, Horowitz SW, Sawlani R, Carroll TJ. Quantitative CBV measurement from static T1 changes in tissue and correction for intravascular water exchange. *Magn Reson Med* 2006;56(1):138–145.
- Srouf JM, Shin W, Shah S, Sen A, Carroll TJ. SCALE-PWI: A pulse sequence for absolute quantitative cerebral perfusion imaging. *J Cereb Blood Flow Metab* 2011;31(5):1272–1282.
- Pan Y, Xia Y. Ultimate Reconstruction: Understand Your Bones From Orthogonal Views. 2021 IEEE 18th Int Symp Biomed Imaging ISBI, 2021, 1155–1158.
- Cohen JP, Luck M, Honari S. Distribution Matching Losses Can Hallucinate Features in Medical Image Translation. In: Frangi AF, Schnabel JA, Davatzikos C, Alberola-López C, Fichtinger G, eds. *Med Image Comput Comput Assist Interv MICCAI* 2018. Cham: Springer International Publishing, 2018; 529–536.

15. He K, Zhang X, Ren S, Sun J. Deep Residual Learning for Image Recognition. arXiv 1512.03385 [preprint] <https://arxiv.org/abs/1512.03385>. Posted December 10, 2015. Accessed July 18, 2022.
16. Kingma DP, Ba J. Adam: A Method for Stochastic Optimization. arXiv 1412.6980 [preprint] <https://arxiv.org/abs/1412.6980>. Posted December 22, 2014. Accessed January 11, 2023.
17. Nilsson J, Akenine-Möller T. Understanding SSIM. arXiv 2006.13846 [preprint] <https://arxiv.org/abs/2006.13846>. Posted June 24, 2020. Accessed January 11, 2023.
18. Sanders JW, Chen HSM, Johnson JM, et al. Synthetic generation of DSC-MRI-derived relative CBV maps from DCE MRI of brain tumors. *Magn Reson Med* 2021;85(1):469–479.
19. Boxerman JL, Shiroishi MS, Ellingson BM, Pope WB. Dynamic Susceptibility Contrast MR Imaging in Glioma: Review of Current Clinical Practice. *Magn Reson Imaging Clin N Am* 2016;24(4):649–670.
20. Ellingson BM, Bendszus M, Boxerman J, et al. Consensus recommendations for a standardized Brain Tumor Imaging Protocol in clinical trials. *Neuro-oncol* 2015;17(9):1188–1198.
21. Inglese M, Ordidge KL, Honeyfield L, et al. Reliability of dynamic contrast-enhanced magnetic resonance imaging data in primary brain tumours: a comparison of Tofts and shutter speed models. *Neuroradiology* 2019;61(12):1375–1386.
22. Grade M, Hernandez Tamames JA, Pizzini FB, Achten E, Golay X, Smits M. A neuroradiologist's guide to arterial spin labeling MRI in clinical practice. *Neuroradiology* 2015;57(12):1181–1202.
23. Ewing JR, Bagher-Ebadian H. Model selection in measures of vascular parameters using dynamic contrast-enhanced MRI: experimental and clinical applications. *NMR Biomed* 2013;26(8):1028–1041.
24. Dhariwal P, Nichol A. Diffusion Models Beat GANs on Image Synthesis. arXiv 2105.05233 [preprint] <https://arxiv.org/abs/2105.05233>. Posted May 11, 2021. Accessed January 11, 2023.